Tidal Pressure Response and Surveillance of Water Encroachment

K. Langaas, SPE, Norske Shell AS; **K.I. Nilsen,** Norwegian Petroleum Directorate; and **S.M. Skjaeveland,** SPE, U. of Stavanger

Summary

A review of the tidal response in petroleum reservoirs is given. Tidal response is caused by periodic changes in overburden stress induced by the ocean tide; the "tidal efficiency factor" is derived by two different approaches and is in line with a recent well test in the Ormen Lange gas field.

For small geomechanical pertubations like the tidal effect, we show that a simplified coupling of geomechanics and fluid flow is possible. The coupling is easy to implement in a standard reservoir simulator by introducing a porosity varying in phase with the tide. Simulations show very good agreement with the theory.

The observation of the tidal response in petroleum reservoirs is an independent information provider [i.e., it provides information in addition to the (average) pressure and its derivative from a well test]. The implementation of the tidal effect in a normal reservoir simulator gives us the opportunity to study complex multiphase situations and to evaluate the potential of the tidal response as a reservoir-surveillance method. The case studies presented here focus on the possibility of observing water in the near-well region of a gas well.

Introduction

The main objective of this work is to investigate whether the tidal pressure response in petroleum reservoirs can be used for reservoir surveillance, in particular to detect saturation changes in the near-well region (e.g., to detect water encroachment toward a gas well). The literature seems sparse in this area. Also, our approach of simplified coupling of geomechanics and fluid flow for small geomechanical effects, and the possibility to implement this in a normal reservoir simulator, has not (to our knowledge) been discussed in the literature. Several authors have derived a tidal efficiency factor, but a review and comparison study seems to be missing.

Tidal Effect. The gravitational pull from the moon and the sun works on both the Earth itself, the ocean, and the atmosphere. From a point within the Earth (e.g., inside a petroleum reservoir), the three effects add up to total tidal dilatation Δe_t as a sum of the three independent partial effects. These are the solid-earth tidal dilatation ΔE, the barometric tidal dilatation ΔB, and the ocean tidal dilatation ΔO, and $\Delta e_t = \Delta E + \Delta B + \Delta O$ (Hemala and Balnaves 1986). The components will have a different magnitude (amplitude), efficiency, frequency, and phase (Robinson and Bell 1971).

Tidal Response in Petroleum Reservoirs. During transient well tests, a gauge is placed in the well to continuously record the pressure and temperature. Modern production wells are often equipped with permanent downhole gauges to monitor well and reservoir behavior.

An important part of a transient well test is the shut-in period, when the well is closed in and pressure gradually builds up. If this period is long enough, it is quite common to observe small and periodic pressure variations. These variations occur on a semidiurnal time scale, repeating every half-day. In addition, other variations with similar but longer periods (e.g., daily) may also be seen. The sinusoidal variation in reservoir pressure observed in well-test data coincides with the periodic variation in the gravitational pull on the Earth by the moon and the sun. In transient-well-test analysis, the tidal effect appears as unwelcome perturbations troubling the interpretation, mainly at the late time periods.

At a reservoir located below the seafloor, the three tidal mechanisms discussed are active at the rock/fluid systems. However, the ocean tide is, by the magnitude of its effects on the reservoir, the dominant source of perturbation (Hemala and Balnaves 1986). The tide gives a certain pressure variation on the seafloor. A much smaller pressure variation is observed in the reservoir. The ratio of the pressure variation at these two locations is known as the tidal efficiency factor. It is discussed further below.

The first observations of the tidal phenomenon in porous media date to the 1880s. The majority of the observations were made in mines and open water wells in which even the smallest periodic fluctuation of water level was easily detectable and recordable (McKee et al. 1990). The effect was first detected in petroleum reservoirs with the advent of highly sensitive pressure gauges. Kuruana (1976) presented the first work relating the periodical pressure oscillation during testing of wells in the Timor Sea with the ocean tides. Arditty et al. (1978) developed a theory that described the pressure variation in closed well systems caused by Earth tides and studied the parameters that determined the amplitude. Hemala and Balnaves (1986) provided an overview of tidal effects from the petroleum-engineering point of view and proposed some applications of the effect to predict fluid heterogeneities in reservoirs. McKee et al. (1990) presented a theory for calculating bulk compressibility from the tidal efficiency factor.

Inspired by Hemala and Balnaves' proposal, Wannell and Morrison (1990) suggested a practical method of measuring vertical permeability, and Dean et al. (1994) introduced a method to monitor compaction and compressibility changes in an offshore chalk reservoir by measuring the tidal effect in the reservoir. Netland et al. (1996) published a method for monitoring compaction not limited to a specific reservoir rock through a more complex expression for the compaction modulus. Pinilla et al. (1997) presented a model coupling aspects of geomechanics, tide, and fluid flow in porous media.

Chang and Firoozabadi (2000) showed that the gravitational pull can be used to estimate the total compressibility in a fractured reservoir. Smit and Sayers (2005) presented a general derivation of the tidal efficiency factor and discussed how the tidal response can assist 4D-seismic monitoring.

Theory

Compressibility Definitions. Three types of compressibilities are often cited in the characterization of a porous medium. These are bulk compressibility, C_b, representing the relative change in bulk volume of the medium; solid-grain compressibility, C_{sg}, representing the relative change in matrix volume of the medium; and pore-volume compressibility, C_p, representing the relative change in pore volume.

The most frequently used definitions of compressibility are as follows (Zimmerman 1991; Chen et al. 1995):

$$C_{bc} = -\frac{1}{V_b}\left(\frac{\partial V_b}{\partial p_c}\right)_{p_p}, \quad \ldots\ldots\ldots\ldots\ldots\ldots\ldots\ldots\ldots\ldots\ldots\ldots (1)$$

This paper (SPE 95763) was first presented at the 2005 SPE Annual Technical Conference and Exhibition, Dallas, 9–12 October, and revised for publication. Original manuscript received for review 9 July 2005. Revised manuscript received 29 May 2006. Paper peer approved 12 June 2006.

$$C_{bp} = \frac{1}{V_b}\left(\frac{\partial V_b}{\partial p_p}\right)_{p_c}, \quad \ldots\ldots (2)$$

$$C_{pc} = -\frac{1}{V_p}\left(\frac{\partial V_p}{\partial p_c}\right)_{p_p}, \quad \ldots\ldots (3)$$

$$C_{pp} = \frac{1}{V_p}\left(\frac{\partial V_p}{\partial p_p}\right)_{p_c}, \quad \ldots\ldots (4)$$

and

$$C_{sgc} = C_{sgp} = C_{sg} = \frac{1}{V_p}\left(\frac{\partial V_p}{\partial p_p}\right)_{p_c\Delta(p_c-p_p)=0} \quad \ldots\ldots (5)$$

The first subscript denotes the type of compressibility: *b* for bulk, *p* for pore volume, and *sg* for solid grain. The second subscript represents the changing pressure: *c* for confining and *p* for pore pressure; and the subscript outside of the parenthesis indicates the pressure (pore or confining) to be maintained constant.

The two bulk compressibilities, C_{bc} and C_{bp}, and solid-grain compressibility, C_{sg}, can be measured directly from specimen volumetric deformation; C_{bc} is measured under constant pore pressure and changing confining pressure, while C_{bp} is measured under constant confining pressure and changing pore pressure. These two values are not the same, but they often differ only by an insignificant amount (i.e., $C_{bc} \approx C_{bp}$).

The compressibility C_{pp} is normally used for reservoir reserves calculation. This is because it is the pore pressure that most affects the porosity (and, hence, the pore volume) and not the horizontal in-situ stress, which would be equivalent to the confining pressure. In reservoir simulators, C_{pp} describes how the porosity changes with changing pore pressure.

The pore-volume compressibilities (C_{pc} and C_{pp}) can be determined only indirectly through measurement of volumetric changes of the pore fluid.

The relationship between all of the above compressibilities can theoretically be derived if elasticity is assumed (Zimmerman 1991):

$$C_{bp} = C_{bc} - C_{sg},$$

$$C_{pc} = \frac{(C_{bc} - C_{sg})}{\phi},$$

$$\text{and } C_{pp} = \frac{[C_{bc} - (1+\phi)C_{sg}]}{\phi} \quad \ldots\ldots (6)$$

This is just another way of writing the Biot (Chen et al. 1995) correlations:

$$C_{bp} = \alpha C_{bc},$$

$$C_{pc} = \frac{\alpha C_{bc}}{\phi},$$

$$C_{pp} = \frac{(\alpha C_{bc} - \phi C_{sg})}{\phi}, \quad \ldots\ldots (7)$$

where $\alpha = 1 - C_{sg}/C_{bc}$ is called the Biot coefficient.

The Tidal Efficiency Factor. The ratio between the tidal pore pressure response in the reservoir and the tidal pressure change at the sea bottom is referred to as the tidal efficiency factor. In the literature, various expressions for this factor are found. One of the first to make such a correlation was C.E. Jacob (1940) in the field of hydrology. The purpose of this section is to derive this expression from first principles. Later on, the theoretical derived factor will be compared with observed values in an Ormen Lange well test.

The basic assumption to derive the tidal efficiency factor is the model of a linear elastic medium (Fjær et al. 1992). We also assume an isotropic medium and an isothermal process. Then, we have

$$\sigma_{ij} = 2G\varepsilon_{ij} + \lambda e\delta_{ij} + \alpha p_p \delta_{ij}, \quad \ldots\ldots (8)$$

where ε_{ij} and σ_{ij} are the components of the bulk-strain tensor and total-stress tensor, respectively; G is shear modulus defined by $G=E/[2(1+\nu)]$, where E is Young's modulus and ν is the Poisson ratio for the solid skeleton under drained conditions; λ is the Lamé constant that is related to other properties by $\lambda = 2\nu G/(1-2\nu) = 1/C_{bc} - (2/3)G$; δ_{ij} is the Kronecker delta; e is the bulk-volume strain defined by

$$e \equiv \varepsilon_{xx} + \varepsilon_{yy} + \varepsilon_{zz}, \quad \ldots\ldots (9)$$

where the subscripts denote components in the bulk-strain tensor; α is the Biot coefficient. Note that only two of the three engineering constants (G, E, and ν) are independent.

Eq. 8 gives a relation between strain, stress, and pore pressure expressed in terms of stress because stress satisfies the equilibrium equation $\sum_j (\partial\sigma_{ij}/\partial x_j) = 0$. The mean normal stress is defined as

$$\sigma_m \equiv \frac{\sigma_{xx} + \sigma_{yy} + \sigma_{zz}}{3}. \quad \ldots\ldots (10)$$

From Eqs. 8 and 10, substituting for λ, we obtain

$$\sigma_m = \frac{1}{C_{bc}} e - \alpha p_p. \quad \ldots\ldots (11)$$

Differentiating Eq. 11 gives

$$de = \alpha C_{bc} dp_p + C_{bc} d\sigma_m. \quad \ldots\ldots (12)$$

Now, using Eq. 7 and the fact that $de \equiv dV_b/V_b$ (Chen et al. 1995) gives

$$\frac{dV_b}{V_b} = C_{bp} dp_p + C_{bc} d\sigma_m. \quad \ldots\ldots (13)$$

This is an expression for a relation between the pressure response in a porous medium and the change in mean normal stress from a linear-elastic-medium model.

Alternatively, we may derive this expression by realizing that the bulk volume is a function of both confining pressure and pore pressure. Then, we have

$$\frac{dV_b}{V_b} = \left(\frac{1}{V_b}\frac{\partial V_b}{\partial p_c}\right)_{p_p} dp_c + \left(\frac{1}{V_b}\frac{\partial V_b}{\partial p_p}\right)_{p_c} dp_p = C_{bp} dp_p - C_{bc} dp_c. \quad (14)$$

Eqs. 13 and 14 are equal for $d\sigma_m = -dp_c$, in line with Chen et al. (1995), whose sign convention we also follow: stress and strain are taken positive in tension, whereas fluid pressure is positive for compression.

We also need an expression for the change in pore-volume strain. A similar derivation as for Eq. 14 gives

$$de_p \equiv \frac{dV_p}{V_p} = C_{pp} dp_p - C_{pc} dp_c. \quad \ldots\ldots (15)$$

At isothermal conditions, the fluid density is a function only of pore pressure, $\rho = \rho(p)$. Assuming a constant fluid mass, it follows that

$$de_f \equiv \frac{dV_f}{V_f} = \frac{1}{V_f}\frac{dV_f}{dp_p} dp_p = -C_f dp_p. \quad \ldots\ldots (16)$$

In a reservoir, the fluid will fill the pore volume completely, and any change in the pore volume implies a change in fluid volume. Therefore, by setting $de_f = de_p$, we obtain an expression for the tidal efficiency factor:

$$\frac{dp_p}{d\sigma_m} = -\frac{C_{pc}}{C_f + C_{pp}}. \quad \ldots\ldots (17)$$

If we instead (as some authors may have done) set $de_f = de$, use the definitions for compressibility, and assume that solid-grain compressibility is much smaller than pore compressibility, we obtain

$$\frac{dp_p}{d\sigma_m} = -\frac{\phi C_{pc}}{C_f + \phi C_{pp}}. \quad \ldots\ldots (18)$$

Eqs. 17 and 18 are the two basic expressions for the tidal efficiency factor found in the literature. We think that Eq. 17 is more valid than Eq. 18.

The change in mean normal stress is not necessarily the same as change in tidal load. Usually, one assumes no damping (i.e., that the mean normal stress amplitude is the same as the sea-bottom tide pressure amplitude $d\sigma_m = -dp_{tide}$). It is common in oilfield compaction studies to assume a uniaxial description (i.e., that the compaction is only in the vertical direction and that the strain in the horizontal directions is zero) (Dean et al. 1994).

Chen et al. (1995) showed that C_{pc} and σ_m will be different for different boundary conditions. For the uniaxial case, $\sigma_m = \sigma_{zz}$, and C_{pc} is replaced by $(1+\nu)/[3(1-\nu)]C_{pc}$; for the biaxial case, $\sigma_m = (\sigma_{yy} + \sigma_{zz})/2$, and C_{pc} is replaced by $\frac{2}{3}(1+\nu)C_{pc}$; and for the triaxial case, $\sigma_m = (\sigma_{xx}+\sigma_{yy}+\sigma_{zz})/3$, and the compressibility is just C_{pc}. Solid-grain compressibility is assumed to be much smaller than pore compressibility in these relations. The expression without this assumption is shown in Pinilla et al. (1997) and Smit and Sayers (2005). Thus, for the uniaxial case, Eq. 17 can be written as

$$\frac{dp_p}{d\sigma_{zz}} = -\frac{1+\nu}{3(1-\nu)}\frac{C_{pc}}{C_f + C_{pp}}. \quad \ldots\ldots\ldots\ldots (19)$$

Dean et al. (1994) write $d\sigma_m = (1+\nu)/[3(1-\nu)]d\sigma_{zz}$ and keep C_{pc} as it is.

As mentioned, different expressions for $dp_p/d\sigma_m$ have been suggested in the literature, most of them as Eq. 17 or Eq. 18. McKee et al. (1990), Jacob (1940), Dean et al. (1994), Netland et al. (1996), and Pinilla et al. (1997) suggest Eq. 17; they all assume that the change in pore strain is equal to the change in fluid strain. Not all these papers specify the equation for the different conditions, but most of them do. Wannell and Morrison (1990) end up with Eq. 18. No damping of the signal is discussed, but using porosity as a damping factor gives good results when comparing with observed data.

Simplified Coupling of Geomechanics and Fluid Flow. Following Chen et al. (1995), for the conservation of fluid mass, we have

$$\nabla \cdot (\rho\phi\mathbf{v}) + \frac{\partial(\phi\rho)}{\partial t} = 0, \quad \ldots\ldots\ldots\ldots (20)$$

and for the solid mass,

$$\nabla \cdot [\rho_s(1-\phi)\mathbf{v}_s] + \frac{\partial[(1-\phi)\rho_s]}{\partial t} = 0. \quad \ldots\ldots\ldots\ldots (21)$$

Furthermore, Darcy's law states that

$$\phi(\mathbf{v} - \mathbf{v}_s) = -\frac{k}{\mu}\nabla p_p. \quad \ldots\ldots\ldots\ldots (22)$$

Inserting Eq. 22 into Eq. 20 and assuming no solid-mass transport ($\mathbf{v}_s = 0$) gives

$$\nabla \cdot \left(\rho\frac{k}{\mu}\nabla p_p\right) = \phi\rho\nabla\cdot\mathbf{v}_s + \frac{\partial(\phi\rho)}{\partial t}. \quad \ldots\ldots\ldots\ldots (23)$$

Eq. 21, with $\mathbf{v}_s = 0$, may be written as

$$\nabla\cdot\mathbf{v}_s = -\frac{1}{\rho_s(1-\phi)}\frac{d[(1-\phi)\rho_s]}{dt}, \quad \ldots\ldots\ldots\ldots (24)$$

and because the solid mass is constant and $(1-\phi)$ is equal to solid volume divided by bulk volume, Eq. 24 becomes

$$\nabla\cdot\mathbf{v}_s = \frac{1}{V_b}\frac{dV_b}{dt}. \quad \ldots\ldots\ldots\ldots (25)$$

Further, inserting Eq. 25 into Eq. 23, we obtain

$$\nabla\cdot\left(\rho\frac{k}{\mu}\nabla p_p\right) = \phi\rho\frac{1}{V_b}\frac{dV_b}{dt} + \frac{d(\phi\rho)}{dt}. \quad \ldots\ldots\ldots\ldots (26)$$

The right-most term of Eq. 26 can be written as

$$\frac{d(\phi\rho)}{dt} = \phi\rho\left(\frac{1}{\rho}\frac{d\rho}{dt} + \frac{1}{\phi}\frac{d\phi}{dt}\right). \quad \ldots\ldots\ldots\ldots (27)$$

Finally, inserting Eq. 27 into Eq. 26 gives

$$\nabla\cdot\left(\rho\frac{k}{\mu}\nabla p_p\right) = \phi\rho\left(\frac{1}{V_b}\frac{dV_b}{dt} + \frac{1}{\rho}\frac{d\rho}{dt} + \frac{1}{\phi}\frac{d\phi}{dt}\right). \quad \ldots\ldots\ldots (28)$$

We now have to identify the dependencies of the different properties. Chen et al. (1995) derived an expression for coupling of fluid flow and geomechanics, and Pinilla et al. (1997) added the tidal effect through a physical approach with porosity dependent on pore pressure p_p and confining pressure p_c, both of which are time dependent. From $\phi = V_p/V_b$, it follows that $(1/V_b)dV_b/dt + (1/\phi)d\phi/dt = (1/V_p)dV_p/dt$. Expanding dV_p on the right side,

$$dV_p = \left(\frac{\partial V_p}{\partial p_c}\right)_{p_p} dp_c + \left(\frac{\partial V_p}{\partial p_p}\right)_{p_c} dp_p, \quad \ldots\ldots\ldots\ldots (29)$$

and with the compressibility definitions (Eqs. 1 through 4), we obtain

$$\frac{1}{V_b}\frac{dV_b}{dt} + \frac{1}{\phi}\frac{d\phi}{dt} = C_{pp}\frac{dp_p}{dt} - C_{pc}\frac{dp_c}{dt}. \quad \ldots\ldots\ldots\ldots (30)$$

Next, we want this physical change to be equal to a change in porosity only. We do this by defining a new porosity, ϕ_{sim}, to be introduced in the numerical reservoir-simulator model by setting

$$\frac{1}{\phi_{sim}}\frac{d\phi_{sim}}{dt} \equiv C_{pp}\frac{dp_p}{dt} - C_{pc}\frac{dp_c}{dt}. \quad \ldots\ldots\ldots\ldots (31)$$

The right sides of Eqs. 30 and 31 are equal, and from Eq. 28, we then obtain the new flow equation

$$\nabla\cdot\left(\rho\frac{k}{\mu}\nabla p_p\right) = \phi\rho\left(\frac{1}{\rho}\frac{d\rho}{dt} + \frac{1}{\phi_{sim}}\frac{d\phi_{sim}}{dt}\right). \quad \ldots\ldots\ldots\ldots (32)$$

This differs from the flow equations of Chen et al. (1995) and Pinilla et al. (1997), who used the change in bulk volume to couple geomechanical and fluid behavior. Here, all the geomechanics is put into an expression for porosity. The remaining task is to find the expression for the new porosity that can be used for implementation in the reservoir simulator.

For tidal effects, p_p and p_c are only time dependent, and we can set $dp_p(t) = \Delta p_p^{const} df(t)$ and $dp_c(t) = \Delta p_c^{const}\, dg(t)$, where superscript 'const' denotes a constant amplitude or pressure change, and $f(t)$ and $g(t)$ are two arbitrary functions of time. Then, Eq. 31 becomes

$$\frac{1}{\phi_{sim}}\frac{d\phi_{sim}}{dt} = C_{pp}\Delta p_p^{const}\frac{df}{dt} - C_{pc}\Delta p_c^{const}\frac{dg}{dt}. \quad \ldots\ldots\ldots\ldots (33)$$

Integrating over time gives

$$\frac{\phi_{sim}(t)}{\phi_0} = \exp[C_{pp}\Delta p_p^{const} f(t) - C_{pc}\Delta p_c^{const} g(t)], \quad \ldots\ldots\ldots (34)$$

where $\phi_0 = \phi_{sim}(t=0)$. Using the Taylor expansion, assuming that the argument of the natural logarithm is small [$\exp(x) \approx 1+x$] and that confining pressure will oscillate, the expression becomes

$$\phi_{sim} = \phi_0\left[1 - C_{pc}\Delta p_c^{const}\sin\left(\frac{2\pi t}{T}\right)\right][1 + C_{pp}\Delta p_p^{const} f(t)]. \quad (35)$$

This is an expression for porosity that needs to be implemented. Here, T is the tidal period, and Δp_c^{const} is the amplitude of the oscillating confining pressure. We have assumed that the only change in the overburden or confining pressure is the tide, but we could also use the expression for compaction of the reservoir over a longer period. The function $f(t)$ takes fluid pressure drop into account. Assuming this to be normalized, Δp_p^{const} is the amplitude of the oscillating pore pressure, and ϕ_0 is the reference porosity. The function $f(t)$ usually will be very small compared to the confining-pressure part; see below for comparison of the two terms using Ormen Lange data. Eq. 35 is the key result that has been implemented in the reservoir simulator. (For simplicity, we have

assumed a constant amplitude of the confining pressure $\Delta p_c^{\text{const}}$. However, the theory and implementation are not limited to this.)

Tidal Pressure Response as a Function of Fluid Saturation and Pressure. The fluid pressure response to a stress change is a function of pore compressibility, fluid compressibility, and stress change. Eq. 17 can be expressed as

$$dp_p = -\frac{C_{pc}}{C_f + C_{pp}} d\sigma_m. \quad \ldots\ldots (36)$$

The fluid compressibility, C_f, is a function of the compressibilities of the fluids in the system and the relative amount of each,

$$C_f = C_g S_g + C_o S_o + C_w S_w, \quad \ldots\ldots (37)$$

where S_g, S_o, and S_w are gas, oil, and water saturations, respectively, and C_g, C_o, and C_w are gas, oil, and water compressibilities, respectively. This follows from the definition of fluid compressibility, $(1/V_f)dV_f/dp_p$, knowing that $V_f = V_w + V_o + V_g$. Thus, the same stress field creates different pressure responses for fluids with different compressibilities. For a gas/water system, we can simplify Eq. 36 and Eq. 37, respectively, as

$$dp_p \approx -\frac{C_{pc}}{C_f} d\sigma_m \quad \ldots\ldots (38)$$

and

$$C_f \approx C_g S_g \quad \ldots\ldots (39)$$

because $C_p << C_g$ and $C_w << C_g$. Thus, having a waterflooded area with $S_w = 0.75$ and a gas area with $S_w = 0.25$, the pressure response in the waterflooded area will be three times that in the gas area. Further, because the gas compressibility is highly dependent on pressure $C_g(p)$, the tidal pressure response for a system with gas present will also vary with reservoir pressure p:

$$dp_p \approx -\frac{C_{pc}}{C_g(p) S_g} d\sigma_m. \quad \ldots\ldots (40)$$

Propagation of Information. We make use of the standard analytical solution to the 1D diffusion equation below. In the limit where $C_{bc} << C_f$, we have (Smit and Sayers 2005)

$$\frac{\partial p}{\partial t} = D \frac{\partial^2 p}{\partial x^2}, \quad D = \frac{k}{\mu \phi C_f} \quad \ldots\ldots (41)$$

in one spatial dimension. Here, D is the diffusivity. The solution gives an estimate of the propagation of any pressure perturbation in the reservoir. Solving for a periodic pressure variation of the form

$$\Delta p_c(t) = \Delta p_c^{\text{const}} \sin\left(2\pi \frac{t}{T}\right), \quad \ldots\ldots (42)$$

where T is the period of the imposed signal, gives

$$\Delta p(x, t) = \Delta p_c^{\text{const}} \exp\left(-x\sqrt{\frac{\pi}{TD}}\right) \times \sin\left(2\pi \frac{t}{T} - x\sqrt{\frac{\pi}{TD}}\right). \quad \ldots\ldots (43)$$

It follows that the signal has decayed to a factor δ of its initial magnitude at a distance

$$x_\delta = -(\ln \delta)\sqrt{\frac{TD}{\pi}}. \quad \ldots\ldots (44)$$

Using Ormen Lange data from **Table 1,** with $S_g = 0.8$ and $\delta = 0.1$, we obtain x=439 m. For a two-phase system, the permeability must be multiplied by the relative permeability of gas, which for $S_g = 0.8$ was 0.876 during simulations. This means that any pressure perturbation will travel in the reservoir and that the signal has decayed to 10% some 440 m away from the start position. This propagation of information may imply a potential for using the tidal pressure response in petroleum reservoirs toward reservoir surveillance (e.g., detecting a change in saturation in the near-well region). Below, the potential to detect water influx toward a gas well is studied by means of reservoir simulation.

TABLE 1—TYPICAL ORMEN LANGE DATA

Porosity	0.3
Initial water saturation (6305/4-1 well)	0.4
Initial water saturation (typical production well)	0.2
Initial reservoir pressure at 2913 m true vertical depth (TVD)	289 bar
Gas compressibility (in simulations)	2.80×10^{-3} bar^{-1}
Water compressibility	4.7×10^{-5} bar^{-1}
Pore compressibility, C_{pc}	7.2×10^{-5} bar^{-1}
Tidal amplitude	0.05 bar
Poisson ratio	0.16
Permeability, horizontal	500 md
Permeability, vertical	50 md
Gas viscosity (in simulations)	0.0242 cp
Tidal period	12 hours

Ormen Lange Gas Field

Ormen Lange is a large gas field offshore mid-Norway. The field is developed as a subsea-to-beach concept with a new gas plant at Aukra. Hydro is the developer, and Shell will be the operator. The other partners are Petoro, Statoil, Dong, and ExxonMobil. The planned production start is October 2007.

Remote operation of the field requires tight well and reservoir surveillance. Each well will be equipped with a wet-gas meter and a water-fraction meter, as well as permanent downhole gauges. Information about the free-formation-water encroachment and production is important, and various "information providers" have been identified for water in the well and the near-well region. The starting point of this work was to explore whether the tidal pressure response had some surveillance potential (Nilsen 2004).

Tidal Pressure Response During a Well Test. The latest appraisal well, 6305/4-1, is located in a well-defined fault polygon. A production test was run to obtain information about fault-sealing capacity and to detect possible pressure depletion. The test had a 16-hour main flow period and a 30-hour buildup period. Ahmed (2003) describes the test and the intepretation. **Fig. 1** shows the time derivative of the pressure buildup with a wavy pattern that indicates the periodic tidal pressure response.

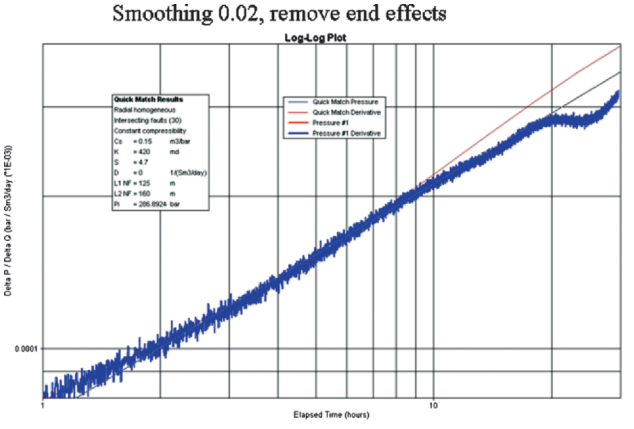

Fig. 1—6305/4-1 well-test data. Time derivative of the pressure vs. elapsed time of the buildup period.

Various methods exist to extract the tidal pressure response. A method independent of our own* confirmed our conclusions of seeing a tidal pressure response with an amplitude of 7.0×10^{-4} to 7.5×10^{-4} bar with a peak at approximately 07:30 hours. Clearly, the tidal pressure response in the Ormen Lange gas is on the borderline of being detectable with today's state-of-the-art pressure-gauge resolution.

Tidal tables indicate a tidal amplitude of approximately 0.5 m with a peak around 07:00 hours during the buildup. This observation supports the presumption that the reservoir pressure reacts without time delay to the tide variation some 2800 m above.

For the simulations and other calculations, we have used the data set in Table 1, which can be representative for Ormen Lange.

The theoretical tidal pressure response follows from Eq. 19. With Table 1 data and 0.4 water saturation, the amplitude is 9.36×10^{-4} bar. This is somewhat higher than the measured value of 7.0×10^{-4} to 7.5×10^{-4} bar. The reasons for this can be many. First of all, there is uncertainty regarding the change in overburden. We have based the estimate on a tide table; to get the correct value of the change in overburden, one needs a pressure gauge on the sea bottom. There is also some uncertainty in the effective Poisson ratio, the compressibilities, and the water saturation. The small Ormen Lange height/width ratio supports the uniaxial-loading assumption.

Implementation in a Reservoir Simulator

MoReS is a reservoir simulator developed and used by Shell (Regtien et al. 1995). It has an inherent programming language that makes it easy to extend the standard functionality. Eq. 35 shows that the tidal effect may be included in a reservoir simulator with a periodic fluctuating porosity. Rewriting Eq. 35 gives

$$\phi_{\text{sim}} = \phi_0\left[1 - C_{pc}\Delta p_c^{\text{const}} \sin\left(\frac{2\pi t}{T}\right)\right](1 + C_{pp}\Delta p_p). \quad \ldots\ldots (45)$$

The right-most parentheses represent the normal dependency of porosity on pressure, automatically implemented in most reservoir simulators (i.e., the linear compaction model). By specifying the pore-volume compressibility in the MoReS input, MoReS will adjust the porosity with changing pressure; porosity increases with increasing pore pressure. The left parenthesis hold the extra term caused by the tide effect.

The normal compaction term will work to modify the porosity perturbation set in the tide term. At a given point in time, the sines function reaches its minimum, giving a maximum porosity. This leads to a lowering of the reservoir pressure, which through the compaction term slightly modifies the porosity downward. The magnitudes of the two terms can be compared from the Ormen Lange data in Table 1. Assuming that the tide stress effect is as for a uniaxial loading, the "tide term" becomes

$$\frac{1+\nu}{3(1-\nu)} C_{pc}\Delta p_c \approx 1.7\times10^{-6}, \quad \ldots\ldots\ldots\ldots\ldots\ldots\ldots (46)$$

which raises the pressure by approximately 1.0×10^{-3} bar. The corresponding "compaction term" becomes

$$C_{pp}\Delta p_p \approx 7.2\times10^{-8}. \quad \ldots\ldots\ldots\ldots\ldots\ldots\ldots\ldots\ldots (47)$$

This shows that the compaction term modifies the porosity perturbation introduced by the tide term by approximately 4%.

To avoid problems in knowing when MoReS applies the compaction term during the range of operations within each timestep, the easy solution is to set the pore-volume compressibility in the MoReS input to zero and apply this compaction term simultaneously with the tide-term function created.

The function was written to implement Eq. 45, updating the porosity at each timestep. The timesteps were kept small, with a maximum timestep length of 10 minutes, because CPU time was not an issue in these simulations.

Simple Reservoir Models. Some simple reservoir models were built to study the tide effect for various scenarios. The 1D model is shown in **Fig. 2,** the 2D model is shown in **Fig. 3,** and the 3D model is shown in **Fig. 4.** The volumes for the three models are the same. Horizontal dimensions are 2000×2000 m, and reservoir height is 50 m. The 1D model is divided into 100 equal grid cells. The 2D and 3D models have local grid refinement so that the block size is recursively halved and ends at a dimension of 6.25 m at the innermost gridblocks. A well is placed at the center of the model. To ensure full symmetry, the well is constructed as a "snake" well perforating all four innermost gridblocks in all layers.

Relative permeabilities and pressure/volume/temperature (PVT) properties were taken from other Ormen Lange reservoir-simulation models.

Consistency Check 1: Simulated vs. Theoretical Response. A homogeneous saturation distribution with $S_w = 0.4$ was used. All grid cells obtained the same pressure fluctuation, and a steady-state situation was established immediately; see **Fig. 5.**

Subtracting the mean value of the fluctuation makes it easier to read the amplitude. **Fig. 6** shows the bottomhole pressure of the well plotted like this.

The theoretical tidal pressure response follows from Eq. 19. With Table 1 data, the amplitude is 9.36×10^{-4} bar. The simulations give 9.3×10^{-4}, which is within the uncertainty of the estimated PVT data (see Fig. 6).

Consistency Check 2: Effect of Saturation. Fig. 7 shows the theoretical and simulated tidal pressure response at different gas saturations given a homogeneous saturation distribution. The theoretical curve follows Eqs. 36 and 37. The match is again within the uncertainty of parameters used for the theoretical curve.

Consistency Check 3: Simulation vs. 1D Analytical Solution. The diffusion of the tidal pressure response can be illustrated by artificially perturbing only the porosity of the left-most grid cell in the 1D model. The model has here a homogeneous saturation with a gas saturation of 0.8. Because of diffusion, the steady-state amplitude in the perturbed cell becomes approximately 15% of its normal size. **Fig. 8** shows the steady-state amplitude in the neighboring cells relative to the left-most cell, together with the predicted decay of the 1D analytical solution, in Eq. 43. The match is excellent. The amplitude (or the information) has decayed to 10% after 440 m. With a gas saturation of 0.6, this distance increases to 505 m.

Simulating Water Influx

Through this extension of a normal reservoir simulator, it is possible to study the tidal pressure response in complex multiphase, fully dynamic situations. To start simple, our approach can be described as "quasistatic," where saturations are kept constant during the simulation. To assist this, the simulations are performed with zero capillary pressure and with the force of gravity turned off. For the timescale of the tidal pressure response (a few days), this is typically a good approximation of a fully dynamic situation.

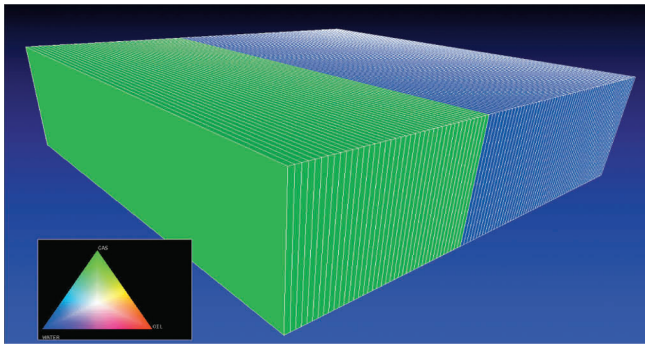

Fig. 2—1D model with gas/water interface.

* Personal communication with P. Lingen, Lingen PL (2003).

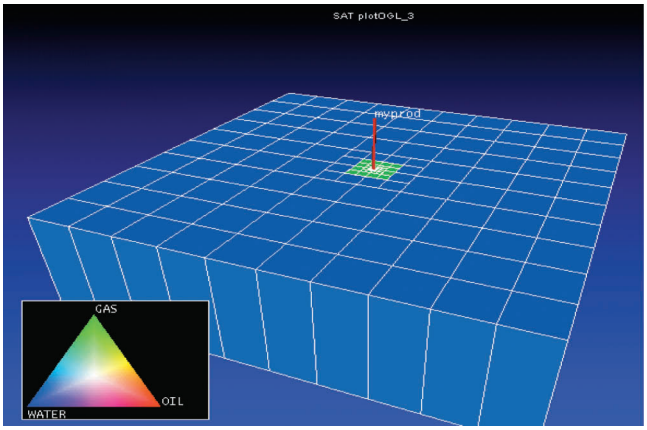

Fig. 3—2D model with water 100 m from the well.

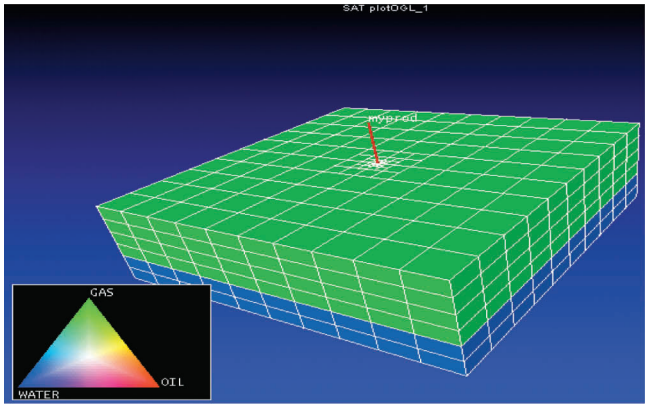

Fig. 4—3D model one-third filled with water.

All scenarios studied here are for a gas/water system. The implementation is equally valid for a three-phase system (oil, gas, water).

Gas/Water Interface in a 1D Model. The typical setup is shown in Fig. 2, with the left part filled with gas. The gas phase has an initial water saturation of 0.2, and the water phase mimics a waterflooded zone with a residual gas saturation of 0.25. The steady-state tidal-pressure-response amplitude is calculated for various volume fractions of gas.

Fig. 9 shows the early-time response in the 10 grid cells closest to the gas/water interface. Here, the gas/water interface is at 100 m (between Cell 5 and Cell 6). A stable steady-state solution is reached within 2 days of simulation time. For this system of only 5% volume of gas, all the grid cells with the gas phase get the same amplitude, but with an amplitude larger than without water in the system. A clear amplitude gradient of approximately 60 m is seen in the water phase.

The steady-state amplitude along the 1D model for this system is shown in **Fig. 10** and labeled "5% gas." Fig. 10 also shows the result from other volume fractions of gas (with a correspondingly changed location of the gas/water interface).

Several important observations can be extracted from this plot. Close to the interface, the gas amplitude has an increased value. With 10% or more gas in the 1D system, the increase in the gas amplitude close to the interface is approximately 10%. The water phase shows a higher reduction in amplitude close to the interface, with an approximately 40% reduction in the grid cell closest to the interface. The amplitude gradient is sharper in the water phase as compared to the gas phase. At some distance from the interface, the water gets an increase in amplitude as compared to the value deep into the water phase (or with only water in the system). The gas seems to get a corresponding reduction in amplitude at some distance from the interface (shown below).

To get a detectable increase in amplitude in the gas phase, the gas volume needs to be small. With 5% (100×2000×50 m) and 3% (60×2000×50 m) gas volume, the maximum gas amplitude increases by 12 and 19%, respectively, as compared to its value with only gas. For the smallest volume (3%), this high value is more or less constant in the gas phase. The 2D and 3D simulations below give some additional insight on this issue.

The fact that the gas phase gets a small decrease in amplitude approximately 400 m from the gas/water interface is shown in **Fig. 11,** which is the reverse of the effect seen in the water phase. For comparison reasons, we have plotted the relative increase in amplitude in the gas phase with the decay of Eq. 43. For a two-phase system with the tide affecting all parts, the decay in amplitude is more rapid than predicted by the 1D analytical solution. The information has decreased to 10% at approximately 250 m from the interface.

Water Encroachment Toward a Gas Well. By simulations, we next want to calculate the tidal pressure response for a gas well

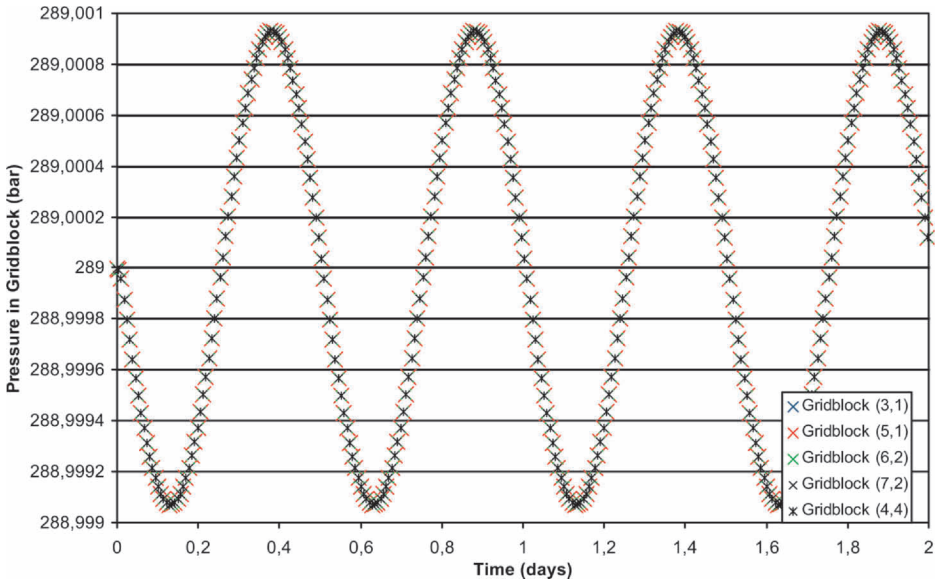

Fig. 5—2D model with homogeneous gas saturation at S_g=0.6. Pressure fluctuation in gridblocks (3,1), (5,1), (6,2), (7,2), and (4,4) during the first 2 days of simulation.

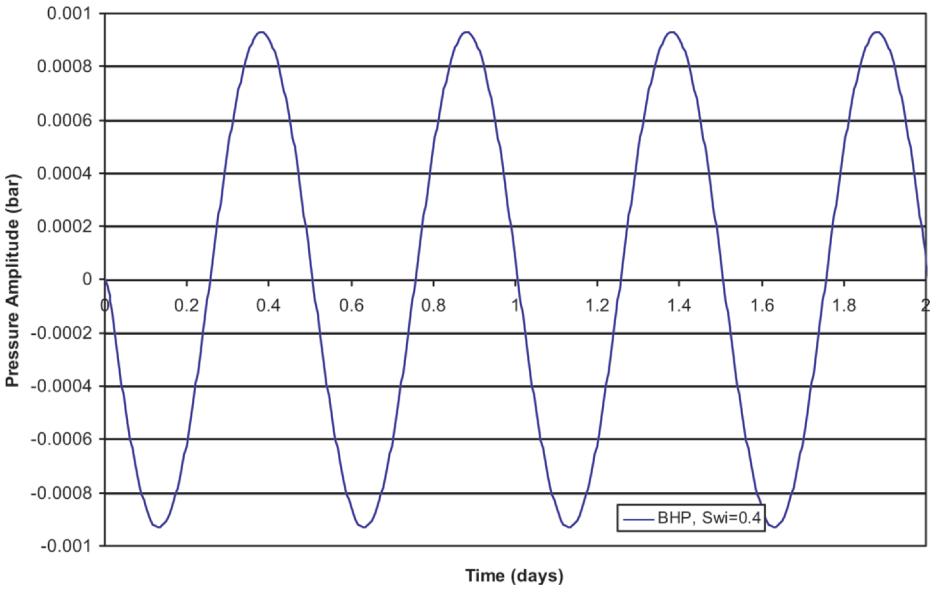

Fig. 6—2D model with homogeneous gas saturation at S_g=0.6. Bottomhole-pressure variation around mean value.

having a water front in the near-well region. Fig. 3 shows the 2D model with water fully surrounding the well (360° encroachment angle) and water 100 m from the well. The simulation is again done in a quasistatic mode, initializing the model with a given saturation distribution. In all cases, the central gas volume is kept quadratic. The encroachment angle is varied between 360 and 90°, as shown in **Fig. 12.**

Fig. 13 shows the tidal-pressure-response amplitude in the gas well as a function of distance to the water front. The distance reported is the closest distance in the grid (e.g., 100 m in Fig. 3). When water is fully surrounding the well like this at full reservoir height, water at a distance of 100 to 200 m may theoretically be detected by means of the increased tidal response in the gas well. With decreasing encroachment angle, the response decreases. Assuming that a 10% increase in amplitude is sufficient, the simulations indicate that water with a 270° encroachment angle can be detected approximately 100 m from the well. Correspondingly, water with a 180° encroachment angle can be detected approximately 50 m from the well. The simulations show that water at a 90° encroachment angle will be hard to detect. At 180 and 270° encroachment angles, the tidal amplitude in the well is not monotonically increasing with decreasing distance to the water. This is probably caused by a balance between the area of the gas/water interface close to the well and the distance to the interface.

It is also of interest to study how the height of the water front affects the tidal pressure response of a gas well. Fig. 4 shows the 3D model with a relative water height of one-third. In the simulation, the water is fully surrounding the well (360° encroachment angle), and the distance to the water (at the closest) is kept at a fixed distance from the well.

Fig. 14 shows the amplitude as a function of relative water height. When the water is close to the well (at 50 m), the simulations suggest a close-to-linear decrease in amplitude with decreasing water height. Including cases with water more distant from the well, the picture becomes a bit more complex. The results may be affected by the gridding and how the well pressure is calculated from the gridblock pressure, as well as vertical permeability (which is kept at 50 md here). Numerical dispersion may have a higher impact in the 3D model, which can explain the small discrepancy between the 2D and 3D results at full water height with water at 100- and 200-m distances. With only gas in the model, the 2D and 3D models give exactly the same result.

Practical Considerations

The tidal pressure response in the Ormen Lange gas field (7.0×10^{-4} to 7.5×10^{-4} bar) is on the borderline of being detectable with today's state-of-the-art pressure-gauge resolution (1×10^{-4} to 2×10^{-4} bar). Consequently, the potential of the tidal pressure response toward reservoir surveillance seems limited. The potential increases with larger tidal amplitude and with hydrocarbon fluid of lower compressibility. The potential will also increase if future pressure gauges come with improved resolution. The "method" is independent of gauge accuracy (which often is less than gauge

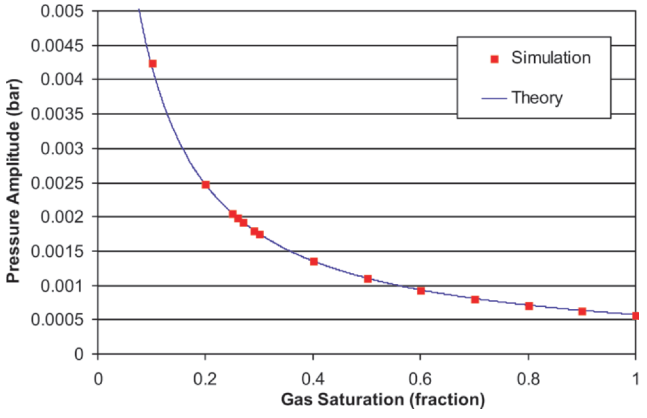

Fig. 7—Theoretical and simulated tidal pressure response at different gas saturations.

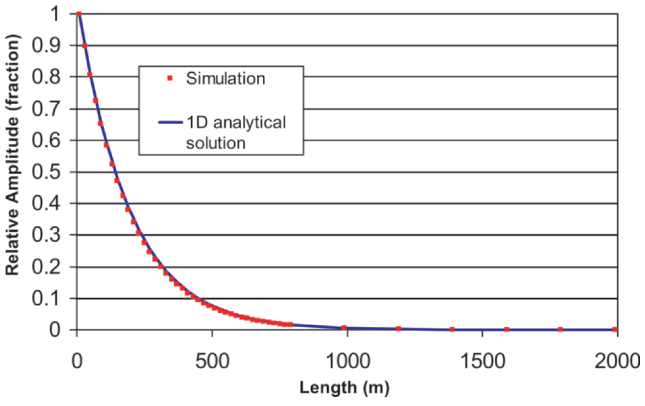

Fig. 8—1D model where the porosity is perturbed in the leftmost cell only. Relative amplitude vs. analytical solution.

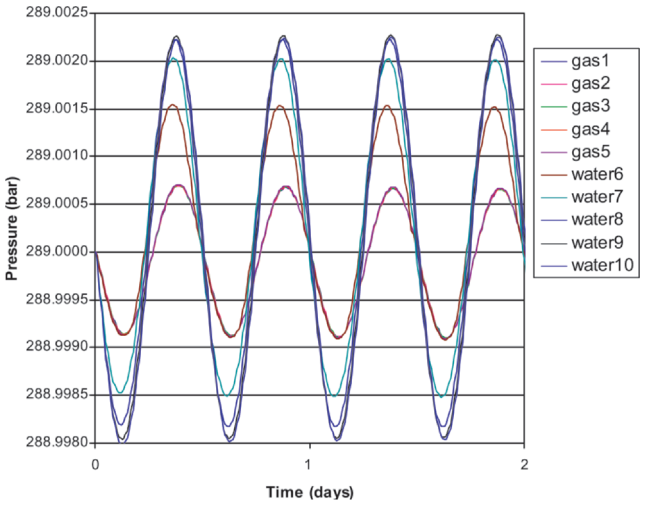

Fig. 9—Tidal pressure response in 1D model around the gas/water interface as a function of simulated time. Gas volume is 5% (interface is between Cell 5 and Cell 6).

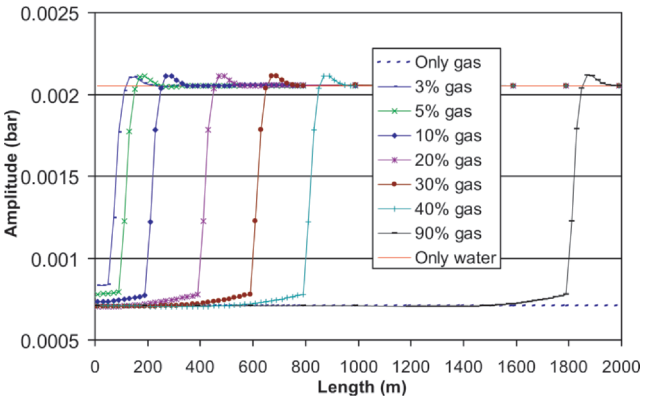

Fig. 10—Tidal-pressure-response amplitude along the 1D model, with various volume fractions of gas.

resolution) because we can extract the tidal pressure response from the relative signal.

Industry experience indicates that tide-table data in general are not accurate enough to derive the periodic change in overburden pressure and that pressure gauges at the sea bottom will be required.* This is especially important for deepwater fields, where changing currents, temperature, and salinity may impact the sea-bottom pressure. Smit and Sayers (2005), however, show a North Sea example in which a tide-table model seeems to be sufficient.

The North Sea example shows also that tides are more complicated than the simple sinusoidal of constant amplitude used in our studies. It is straightforward to include a more realistic overburden change in the above reservoir-simulation setup. For tides with varying amplitude, the periods with largest amplitude will then likely be the periods with largest signal-to-noise ratio.

For any practical implementation, it is important to analyze the expected signal-to-noise ratio. Sources of noise in addition to general system noise can include condensate or liquid fallback in shut-in situations and interference effects with other wells. For gas applications, it is also important to properly account for the pressure effect on gas compressibility $C_g(p)$.

Conclusions

A practical review of the tidal pressure response in petroleum reservoirs is given. An expression for the tidal efficiency factor has been derived, and the calculated tidal pressure response is in line with recent observations from an Ormen Lange well test. The response depends on the saturation distribution in the near-well region and may in principle be used for reservoir surveillance purposes.

A simplified coupling is derived between geomechanics and reservoir-fluid flow, valid for small geomechanical effects. It is shown that the simplified coupling can be implemented correctly in a standard reservoir simulator through a time-dependent porosity function. Several consistency checks show that the implementation works very well.

With the tidal effect incorporated in the reservoir simulator, it is possible to study complex multiphase problems and evaluate the monitoring of the tidal response as a reservoir-surveillance method. We have concentrated on forecasting water encroachment toward Ormen-Lange-type gas wells.

The simulations results show that:

1. With a 1D interface between gas and water, the gas amplitude is typically 10% higher close to the water and drops faster than Eq. 43 away from the interface. If the gas volume is small enough, the amplitude in the gas phase will increase beyond the 10%.
2. With water at full height around the well and a 360° encroachment angle, the tidal response increases rapidly with decreasing distance to the water. Assuming a 10% increase is needed, water at a distance of 100 to 200 m should be detectable. With a lower encroachment angle, water needs to be closer to be detectable (approximately 100 m for 270° and 50 m for 180°).

* Personal communication with J.J. Freeman and R.H. Hite, Shell Intl. E&P (2004).

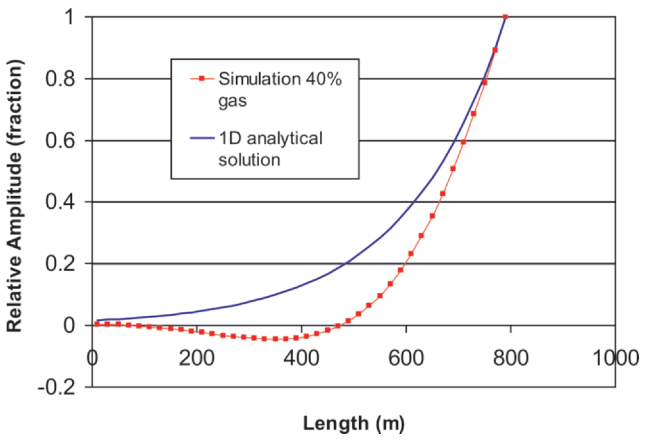

Fig. 11—1D model with 40% gas. Tidal pressure increase in gas phase relative to value at the interface. The 1D analytical model of one-phase diffusion is shown for comparison.

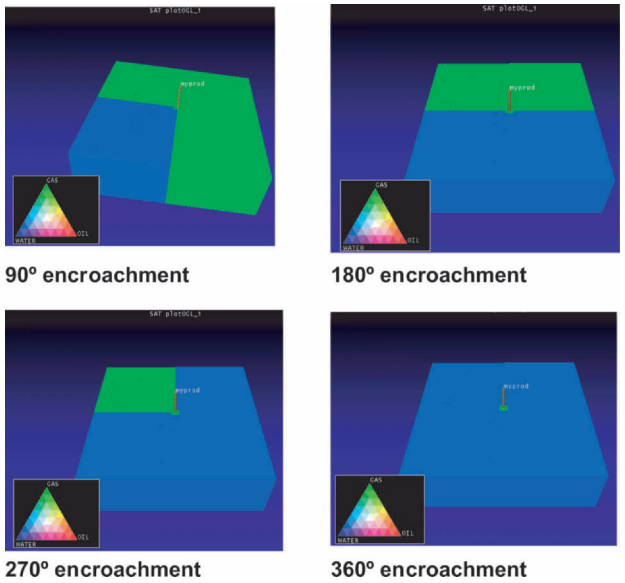

Fig. 12—Water encroachment toward a gas well.

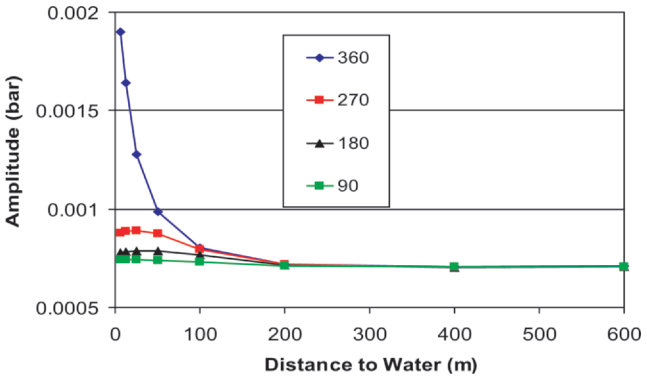

Fig. 13—Amplitude in a gas well as a function of (closest) distance to water; 360°, 270°, 180°, and 90° encroachment angles.

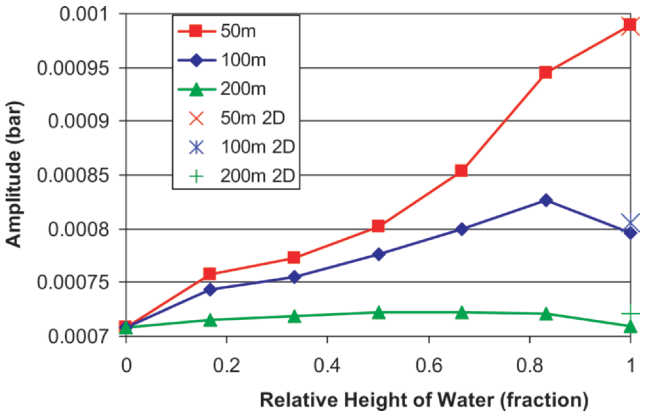

Fig. 14—Amplitude in a gas well as a function of the relative height of approaching water. Closest distance to the water is varied from 50 to 200 m; the result from the 2D model is included.

3. With water at full encroachment but reduced water height, the response seems to decrease roughly linearly with decreasing water height.

The tidal response may carry information on top of the information normally extracted from transient well tests or from pure observation wells. The potential toward reservoir surveillance of a gas/water system is perhaps limited but may increase if future pressure gauges come with higher resolution, and simultaneous observation of tidal responses from many wells could be systemized and correlated in real time. The only additional investment required would be to install pressure gauges at the sea bottom to accurately monitor overburden pressure variations.

Nomenclature

C_{bc} = bulk compressibility with respect to confining pressure with constant pore pressure, Lt^2/m
C_{bp} = bulk compressibility with respect to pore pressure with constant confining pressure, Lt^2/m
C_f = fluid compressibility, Lt^2/m
C_g = gas compressibility, Lt^2/m
C_o = oil compressibility, Lt^2/m
C_{pc} = pore compressibility with respect to confining pressure with constant pore pressure, Lt^2/m
C_{pp} = pore compressibility with respect to pore pressure with constant confining pressure, Lt^2/m
C_{sg} = solid-grain compressibility, Lt^2/m
C_{sgc} = solid-grain compressibility with respect to confining pressure with constant pore pressure, Lt^2/m
C_{sgp} = solid-grain compressibility with respect to pore pressure with constant confining pressure, Lt^2/m
C_w = water compressibility, Lt^2/m
de = change in bulk strain, dimensionless
de_f = change in fluid strain, dimensionless
de_p = change in pore strain, dimensionless
dh = ocean tide amplitude measured in length, L
D = diffusivity, L^2/t
e = bulk volume strain, dimensionless
E = Young's modulus, m/Lt^2
$f(t)$ = arbitrary function of time, dimensionless
g = Earth's gravitational pull, L/t^2
$g(t)$ = arbitrary function of time, dimensionless
G = shear modulus, m/Lt^2
k = permeability, L^2
p_c = confining pressure, m/Lt^2
p_p = pore pressure, m/Lt^2
S_g = gas saturation, fraction
S_o = oil saturation, fraction
S_w = water saturation, fraction
t = time, t
T = period of imposed signal, t
$\mathbf{v}$ = fluid velocity vector, L/t
$\mathbf{v}_s$ = solid velocity vector, L/t
V_b = bulk volume, L^3
V_f = fluid volume, L^3
V_p = pore volume, L^3
x = distance, L
α = Biot coefficient defined as $\alpha = 1-C_{sg}/C_{bc}$, dimensionless
δ = decay factor, dimensionless
δ_{ij} = Kronecker delta ($\delta_{ij} = 1$ for $i = j$, $\delta_{ij} = 0$ for $i \neq j$)
ΔB = barometric tidal dilatation, dimensionless
Δe_t = total dilatation, dimensionless
ΔE = Earth tidal dilatation, dimensionless
ΔO = ocean's tidal dilatation, dimensionless
$\Delta p_c^{\text{const}}$ = amplitude of confining-pressure change, m/Lt^2
$\Delta p_p^{\text{const}}$ = amplitude of pore-pressure change, m/Lt^2
ε_{ij} = component of bulk strain, dimensionless
ϕ = porosity, fraction
ϕ_{sim} = porosity used in the simulations, fraction
$\phi_O = \phi_{\text{sim}}(t = 0)$
λ = Lamé's constant, m/Lt^2
μ = viscosity, m/Lt
ν = Poisson's ratio, dimensionless
ρ = fluid density, m/L^3
ρ_s = solid density, m/L^3
σ_{ij} = component of total stress, m/Lt^2
σ_m = mean normal stress, m/Lt^2

Acknowledgments

We would especially like to thank P. Lingen, J.J. Freeman, R.H. Hite, and D. Smit for their valuable input to this study. We would also like to thank Shell and the Ormen Lange partners for the permission to publish.

References

Ahmed, I. 2003. Use of Finite Difference Sector Model to Analyse Well Test in the Ormen Lange Gas Field. Paper SPE 83966 presented at the Offshore Europe Conference, Aberdeen, 2–5 September.

Arditty, P.C., Ramey, H.J. Jr., and Nur, A.M. 1978. Response of a Closed Well-Reservoir System to Stress Induced by Earth Tides. Paper SPE 7484 presented at the SPE Annual Technical Conference and Exhibition, Houston, 1–3 October.

Chang, E. and Firoozabadi, A. 2000. Gravitational Potential Variations of the Sun and Moon for Estimation of Reservoir Compressibility. *SPEJ* **5** (4): 456–465. SPE-67952-PA.

Chen, H.-Y., Teufel, L.W., and Lee, R.L. 1995. Coupled Fluid Flow and Geomechanics in Reservoir Study—I. Theory and Governing Equa-

tions. Paper SPE 30752 presented at the SPE Annual Technical Conference and Exhibition, Dallas, 22–25 October.

Dean, G.A., Hardy, R., and Eltvik, P. 1994. Monitoring Compaction and Compressibility Changes in Offshore Chalk Reservoirs. *SPEFE* **9** (1): 73–76. SPE-23142-PA.

Fjær, E., Holt, R.M,, Horsrud, P., Raaen, A.M., and Risnes, R. 1992. *Petroleum Related Rock Mechanics.* Amsterdam: Elsevier Science Publishers.

Hemala, M.L. and Balnaves, C. 1986. Tidal Effect in Petroleum Well Testing. Paper SPE 14607 presented at the SPE Offshore South East Asia Show, Singapore, 28–31 October.

Jacob, C.E. 1940. On the flow of water in an elastic artesian aquifer. *Trans.,* Am. Geophys. Union, part 2, 574–586.

Kuruana, A.K. 1976. Influence of Tidal Phenomenon on Interpretation of Pressure Build Up and Pulse Test. *APEA J.* **16:** Part I.

McKee, R.C, Bumb, A.C., and Horner, D.A. 1990. Use of Barometric Response To Obtain In-Situ Compressibility of a Coalbed Methane Reservoir. *SPEFE* **5** (2): 167–170; *Trans.,* AIME, **289.** SPE-17725-PA.

Netland, S.O., Knapstad, B., and Holt, R.M. 1996. Estimation of In Situ Compaction Modulus From Tidal Response in Well Test Data. Paper SPE 36821 presented at the SPE European Petroleum Conference, Milan, 22–24 October.

Nilsen, K.I. 2004. Theory of the Tidal Response in Petroleum Reservoirs and Evaluation of Its Potential Towards Reservoir Surveillance. MS thesis, U. of Stavanger.

Pinilla, J.F., Trevisan, O.V., and Tinoco, F.L. 1997. Coupling Reservoir and Geomechanics to Interpret Tidal Effects in a Well Test. Paper SPE 38939 presented at the SPE Annual Technical Conference and Exhibition, San Antonio, Texas, 5–8 October.

Regtien, J.M.M., Por, G.J.A, van Stiphout, M.T., and van der Vlugt, F.F. 1995. Interactive Reservoir Simulation. Paper SPE 29146 presented at the SPE Reservoir Simulation Symposium, San Antonio, Texas, 12–15 February.

Robinson, E.S. and Bell, R.T. 1971. Tides in confined well aquifer systems. *J. Geophysical Research* **76** (8): 1857–1869.

Smit, D. and Sayers, C.M. 2005. Can tidal-driven pressure changes reveal reservoir properties for use in 4D monitoring. *World Oil* (March 2005) 37–43.

Wannell, M.J. and Morrison, S.J. 1990. Vertical Permeability Measurement in New Reservoirs Using Tidal Pressure Changes. Paper SPE 20532 presented at the SPE Annual Technical Conference and Exibition, New Orleans, 23–26 September.

Zimmerman, R.W. 1991. *Compressibility of Sandstones.* Amsterdam: Elsevier Science Publishers.

SI Metric Conversion Factors

bar × 1.0*	E+05	= Pa
ft × 3.048*	E–01	= m

*Conversion factor is exact.

Kåre Langaas is a senior reservoir engineer at Norske Shell AS. e-mail: kare.langaas@shell.com. He holds a PhD degree in physics from the U. of Bergen and an MS degree in petroleum engineering from the U. of Stavanger. **Knut Ingvar Nilsen** is a reservoir engineer at The Norwegian Petroleum Directorate. e-mail: Knut-Ingvar.Nilsen@npd.no. He holds an MS degree in petroleum engineering from the U. of Stavanger. **Svein M. Skjaeveland** is Head of the Dept. of Petroleum Engineering at the U. of Stavanger and a professor of reservoir engineering. e-mail: s-skj@ux.uis.no. He holds PhD degrees in, respectively, physics from the Norwegian Inst. of Technology and petroleum engineering from Texas A&M U.